




## Open Archive Toulouse Archive Ouverte (OATAO)

OATAO is an open access repository that collects the work of Toulouse researchers and makes it freely available over the web where possible

This is an author's version published in: <http://oatao.univ-toulouse.fr/23531>

**Official URL:** <https://doi.org/10.1016/j.actamat.2015.01.016>

### To cite this version:

Caillard, Daniel and Martin, Rautenberg  and Feaugas, Xavier *Dislocation mechanisms in a zirconium alloy in the high-temperature regime: An in situ TEM investigation.* (2015) *Acta Materialia*, 87. 283-292. ISSN 1359-6454

Any correspondence concerning this service should be sent to the repository administrator: [tech-oatao@listes-diff.inp-toulouse.fr](mailto:tech-oatao@listes-diff.inp-toulouse.fr)

# Dislocation mechanisms in a zirconium alloy in the high-temperature regime: An *in situ* TEM investigation

Daniel Caillard,<sup>a,\*</sup> Martin Rautenberg<sup>b</sup> and Xavier Feugas<sup>c</sup>

<sup>a</sup>CEMES/CNRS, BP 94347, 31055 Toulouse Cedex 4, France

<sup>b</sup>CIRIMAT, CNRS/UPS/INPT, 4 allée Emile Monso, 31030 Toulouse, France

<sup>c</sup>LaSIE/CNRS, Université de La Rochelle, avenue Michel Crépeau, 17042 La Rochelle, France

**Abstract**—Dislocation mechanisms responsible for the high-temperature mechanical properties of a Zr alloy have been investigated using *in situ* straining experiments between 250 °C and 450 °C. At 250 °C and 300 °C, the results show a steady and homogeneous dislocation motion in prismatic planes, with little cross-slip in the pyramidal and/or basal planes. At 350 °C, the kinetics of mobile dislocations becomes very jerky and inhomogeneous, in agreement with a dynamic strain aging mechanism. Above this temperature, the motion is again steady and homogeneous. Extensive cross-slip forms super-jogs which are efficient pinning points against the glide motion. These super-jogs move by glide along the Burgers vector direction, never by climb. The glide velocity between super-jogs is linear as a function of the total driving stress (applied stress minus line-tension stress due to dislocation curvature), in agreement with the solute dragging mechanism. The origin of the stress–strain rate dependence with an exponent larger than unity is then discussed.

**Keywords:** Zirconium; Dislocations; *In situ* transmission electron microscopy; High temperature creep

## 1. Introduction

The origin of the high-temperature mechanical properties of Zr- $\alpha$  and Zr alloys ( $T > 200$  °C) are still the subject of deep confusion and intricate controversies, although abundant experimental results are available and look most often fairly consistent.<sup>1</sup> The reason for this unsatisfying situation is obviously that the dislocation mechanisms likely to occur above room temperature are not sufficiently understood. Different interpretations found in the literature are all based on the analysis of the temperature dependence (activation energy), stress dependence (activation volume, power-law exponent) of the deformation rate and *post-mortem* TEM observations [1–21].

The temperature dependence will not be discussed here. Indeed, the activation energies measured in creep and constant strain-rate tests are very scattered, and no reliable conclusion can emerge from their comparison with various diffusion energies (also not accurately known). The stress dependence is much more informative, and most interpretations are actually based on the study of either activation volumes or stress exponents of the stress–strain rate dependence.

As shown below, two types of interpretations emerge from two types of experiments: whereas thermally activated glide is the natural interpretation of constant strain-rate tests, either climb-controlled recovery or thermally activated glide is proposed in creep tests. In other words, thermally activated glide may be the only mechanism involved in constant strain-rate and creep if both tests are considered to be not fundamentally different (apart from their different strain rates), but climb-controlled recovery may be rate-controlling in creep in the alternative case. The detailed results of both kinds are listed below.

– Relaxation tests in constant strain-rate experiments yield activation volumes which all have the same variation as a function of temperature: an increase from  $\sim 25 b^3$  at 200 °C to a peak at  $\sim 350$  °C, followed by a decrease to  $\sim 50 b^3$  at 400 °C [1–5]. The peak, to which corresponds a plateau in the stress versus temperature curve, is unanimously interpreted by the occurrence of dynamic strain aging (DSA) [1–8]. Note that several creep studies also conclude that DSA takes place in the same temperature range ([9,10], see below). Below the peak, the controlling mechanism has been proposed to be the crossing of solute atoms (solid solution strengthening) according to [1,2]. Above the peak, the controlling mechanism is unclear but has been proposed to be the climb of jogs on screw dislocations by [1].

\* Corresponding author.

<sup>1</sup>The same comment can also be made for Ti- $\alpha$  and Ti alloys.

– Creep tests yield the stress exponent of the minimum creep rate versus stress dependence,  $n \sim 6$ , in average. However, two sets of measurements and corresponding interpretations can be distinguished: (i)  $n$  independent of stress [11–13], interpreted in terms of classical climb-recovery controlled mechanisms, and (ii)  $n$  increasing with increasing stress [14,15], interpreted by some thermally activated glide mechanism, either non-specified [14], or assumed to be the climb of jogs or super-jogs on screw dislocations [15,16]. This second category also includes the results of Rupa [10] showing that  $n \sim 3.7$  at 300 °C, increases to  $\sim 6.6$  at 350 °C, and then decreases to  $\sim 5.2$  at 400 °C, in accordance with the peak of activation volume discussed above.

In brief, two types of mechanisms are likely to occur: (i) the thermally activated glide of dislocations, including DSA at about 350 °C, most often assigned to the climb of jogs/superjogs on screw dislocations, and (ii) the classical recovery-controlled creep where the climb-driven annihilation of dislocations in excess is rate-controlling.

If one considers that the occurrence of DSA is well established, there is however one surprising inconsistency in the corresponding models. Indeed, DSA which is the dynamic interaction between gliding dislocations and mobile solute atoms (the latter tending to catch and pin the dislocations), should be followed by the dragging of solute atoms at higher temperatures. This thermally activated mechanism has however never been assumed to play any role above the DSA domain, probably because its stress dependence ( $n = 1$ ) does not fit with the experimental one ( $n \sim 6$ ). It should however not be completely rejected, and a *minima* be included in, or mixed with other mechanisms.

All these possible mechanisms are so different that they should be easily distinguished from each other, especially in *in situ* straining experiments where both the geometry and the kinetics of dislocation motion can be recorded as a function of stress and temperature. In particular, it should be fairly easy to identify glide or climb motion, as well as the most efficient obstacles to this motion, e.g., pinning points like jogs or solute dragging. Such experiments have been carried out between 250 °C and 450 °C, and the results are presented below.

## 2. Experimental

*In situ* experiments were carried out in a JEOL 2010 HC transmission electron microscope, with a high-temperature straining device developed in the CEMES, and the motion of dislocations was recorded by a Megaview III camera working at 25 images per second.

Cladding tubes and strips of a M5<sup>®</sup> zirconium alloy were provided by AREVA-CEZUS. The tubes were obtained by cold pilgering rolling, followed by heat treatment, inducing a fully recrystallized hexagonal close packed microstructure with a strongly anisotropic crystallographic texture [21]. Grains are isotropic and have a size of 3–5  $\mu\text{m}$ . The chemical composition of the M5<sup>®</sup> [22,23] is given in Table 1. Alloying elements induce homogeneously distributed second phase particles ( $\beta$ -Nb precipitates and Laves phases). Thus, the  $\alpha$ -Zr matrix is mainly alloyed with

oxygen. The oxygen content is quite higher (1507 wppm) than common reactor-grade alloys (1000–1400 wppm).

Microsamples were cut out of tubes, mechanically thinned down and electrolytically polished using a Tenupol 5 and a solution of 70% methanol, 20% 2-butoxyethanol and 10% perchloric acid. They were glued on a copper grid with a high-temperature cement, and strained at a low speed providing a local strain-rate comprised between  $10^{-6}$  and  $10^{-5} \text{ s}^{-1}$ . Seven micro-samples have been successfully strained as a whole (more than 7 h of usable video recording), but the results presented in this article refer to only three grains belonging to two samples. In sample 1 deformed at various temperatures comprised between 250 °C and 450 °C, the observed grain corresponds to a (01 $\bar{1}$ 2) foil plane and near-[ $\bar{2}$ 110] tensile direction. In sample 2 deformed at 400 °C, the first grain corresponds to a (3417) foil plane and near-[2130] tensile direction, and the second grain to a (2535) foil plane and near-[3 $\bar{1}$ 2 $\bar{1}$ ] tensile direction. The local straining axis usually remains within  $\pm 10^\circ$  from the external one, depending on the observed area, in such a way that the applied force on dislocations can be roughly predicted by the Schmid law.

## 3. Results

### 3.1. Geometry and kinetics of glide as a function of temperature

The experimental results described in this section show that three temperature domains can be defined, the intermediate one corresponding to dynamic strain aging. They also give details on the geometry of the high-temperature mechanism, i.e. the multiplication at sources in the prismatic plane, and the pinning and multiplication at super-jogs formed by cross-slip. Lastly, they show that super-jogs move exclusively by glide, never by climb.

A first set of results have been obtained in sample 1 at temperatures increasing from 250 °C to 450 °C. Fig. 1 shows dislocations with Burgers vector  $1/3[1\bar{1}20]$  moving steadily and homogeneously in the thin foil at 250 °C. Many dislocations (e.g.,  $d_2$ ) have a dipolar shape with long segments parallel to the foil surface, resulting from the difficult shearing of the oxide layer. Other dislocations (e.g.,  $d_1$ ) which have sheared the surface more easily trail slip traces (e.g., the straight faint contrast noted trP) parallel to the intersection of the foil surface with the ( $\bar{1}$ 100) prismatic plane, which indicates glide in this plane. Dislocation  $d_1$  is not elongated in any close packed direction, either edge or screw, and its motion is slightly jerky and irregular at the fine scale, as shown in the enlargement of Fig. 2. Indeed, dislocations are often pinned at localized obstacles (as P in Fig. 2a) and move by series of non-correlated unpinning events.

The motion is still homogeneous at 300 °C, as shown in Fig. 3 and no significant difference between screw and edge dislocation mobility can be observed.

**Table 1.** Chemical composition (in weight) of the M5<sup>®</sup>.

Nb (%)	O (ppm)	Fe (ppm)	Cr (ppm)	Zr
1	1507	370	41	Bal.

<sup>2</sup>M5<sup>®</sup> is a trademark of AREVA NP registered in the United States of America and in other countries.

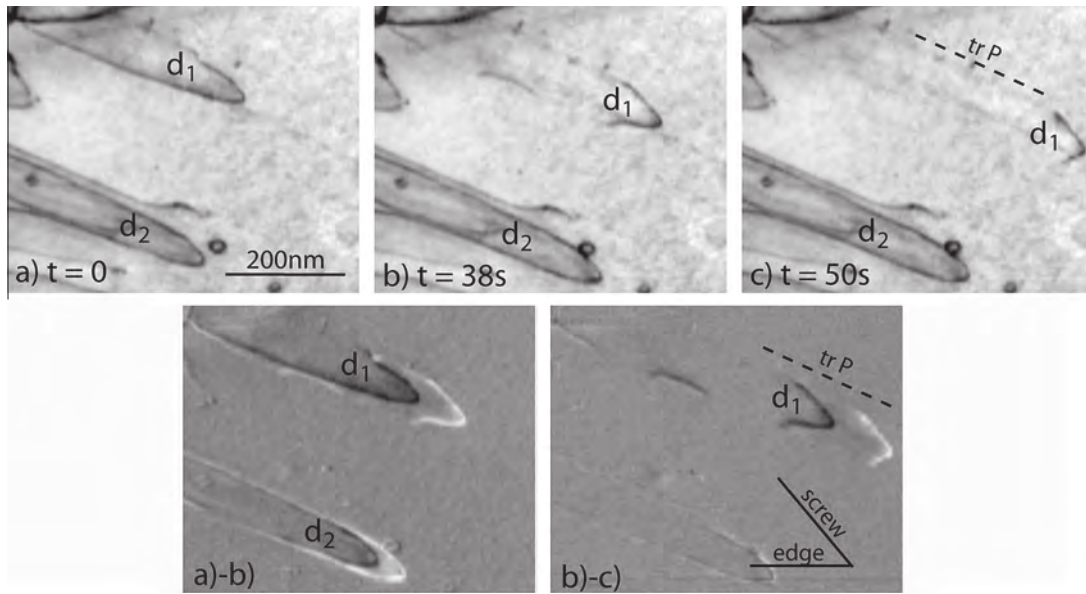


**Fig. 1.** Motion of dislocations  $d_1$  and  $d_2$  in a prismatic plane of sample 1, at 250 °C. The slip trace noted  $trP$  corresponds to the intersection of the prismatic slip plane with the foil surface. The directions noted “edge” and “screw” are the projections of the real directions in the observation plane. Diffraction vector  $(\bar{1}01\bar{1})$ . The corresponding video can be downloaded as a [Supplementary material](#).

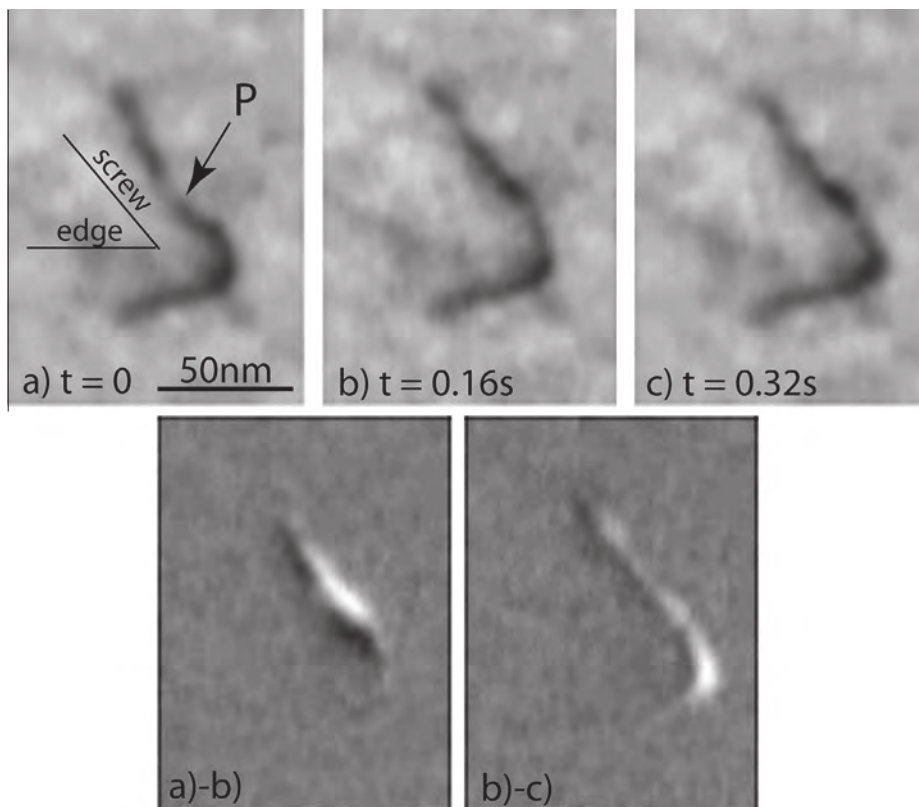


**Fig. 2.** Detail of the motion of dislocation  $d_1$  in [Fig. 1](#). The lower images are differences between the bright-field images at different times of observation. The motion between  $t = 0$  and  $t = 0.16$  s clearly correspond to the crossing of a localized obstacle in  $P$ .

A marked change of kinetics has been observed in all samples (three as a whole, and five grains) strained at 350 °C. [Fig. 4](#) shows the same area as in [Figs. 1–3](#). The same dislocations as in [Fig. 1](#) trailing long dipoles parallel to the surfaces are observed, but their kinetics of motion is

very different. Indeed, all dislocations remain almost immobile whereas only one (noted  $d$ ) starts to move fast (velocity of  $\sim 5 \mu\text{m/s}$ ) and then stops. Deformation thus proceeds by a series of fast motions of a few dislocations, contrary to the homogeneous and steady motion observed at lower

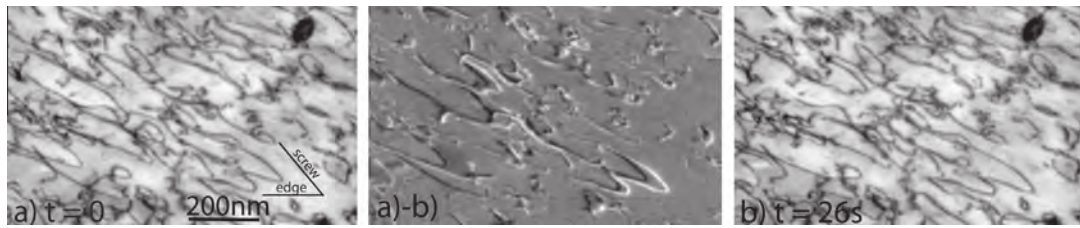


**Fig. 3.** Homogeneous dislocation motion at 300 °C (sample 1, diffraction vector  $(0\bar{1}\bar{1}1)$ ). The corresponding video can be downloaded as a [Supplementary material](#).

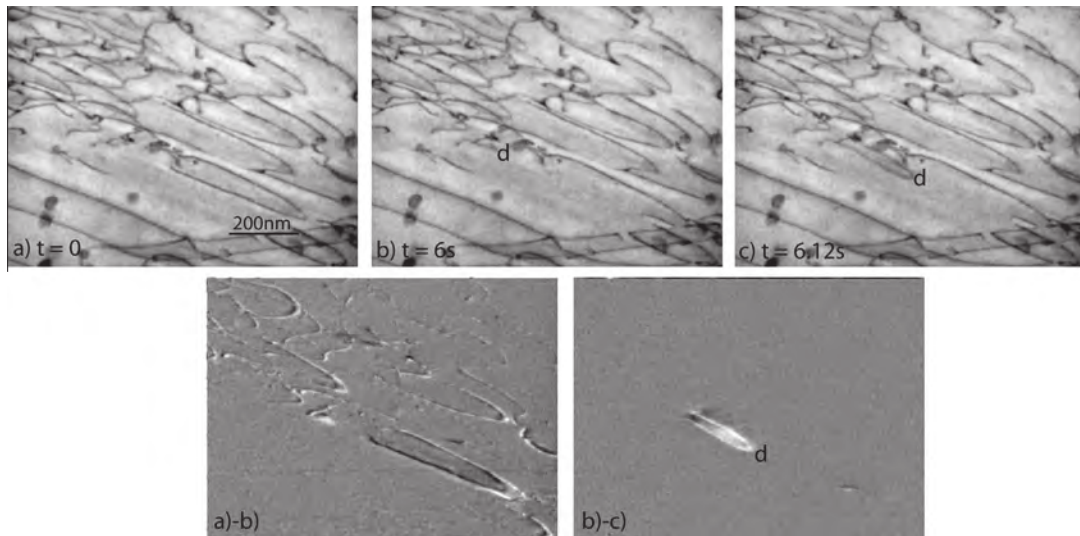


**Fig. 4.** Inhomogeneous dislocation motion at 350 °C (sample 1, diffraction vector  $(\bar{1}0\bar{1}\bar{1})$ ). Note the slow motion of all dislocations between (a) and (b), separated by 6 s, and the fast motion of d between (b) and (c), separated by 0.12 s. The corresponding video can be downloaded as a [Supplementary material](#).

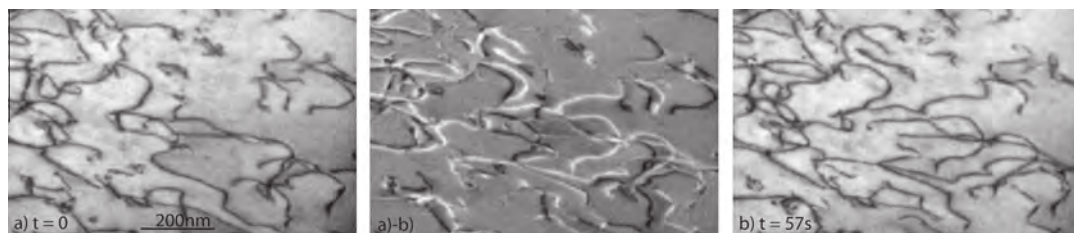


**Fig. 5.** Homogeneous dislocation motion at 450 °C (sample 1, diffraction vector  $(0\bar{1}\bar{1}1)$ ). The corresponding video can be downloaded as a [Supplementary material](#).

temperatures. This motion still takes place mainly in the prismatic plane, although cross-slip in another plane has also been observed.

Above 400 °C, the deformation is again homogeneous, and proceeds by the steady motion of all dislocations at a lower speed. Fig. 5 illustrates this kind of motion where dislocations cross slip extensively between the  $(\bar{1}100)$  prismatic plane and either the  $(\bar{1}10\bar{1})$  pyramidal plane or the  $(0001)$  basal plane, at 450 °C. The motion is however steadier than at 250 °C and 300 °C, as shown in Fig. 6.

A second set of results have been obtained in sample 2 strained at 400 °C, in two grains with two different orientations. In grain 1, dislocations with Burgers vector  $1/3[2\bar{1}\bar{1}0]$  have been observed to glide in their  $(0\bar{1}10)$  prismatic plane. Fig. 7 shows that the slip traces are very recti-

linear, which shows that cross-slip is not activated. Note that in this case, the prismatic system has a higher Schmid factor ( $FS(P) = 0.5$ ) than the most activated first-order pyramidal one ( $FS(\pi) = 0.45$  for  $(0\bar{1}\bar{1}\bar{1})$  and the basal plane ( $FS(B) = 0.05$ ). A dislocation is pinned on a precipitate noted P, and one arm (noted d) rotates in the clockwise direction and emits  $d_1$  to the left and  $d_2$  to the right, in the  $(0\bar{1}10)$  prismatic plane. The moving dislocation has an elliptical shape with no straight part along screw or edge directions. No Orowan loop can be seen after more than 10 rotations around the precipitate P, which shows that they have been absorbed by the matrix-precipitate interface.

The situation is different in grain 2 where dislocations with Burgers vector  $1/3[2\bar{1}\bar{1}0]$  cross slip extensively

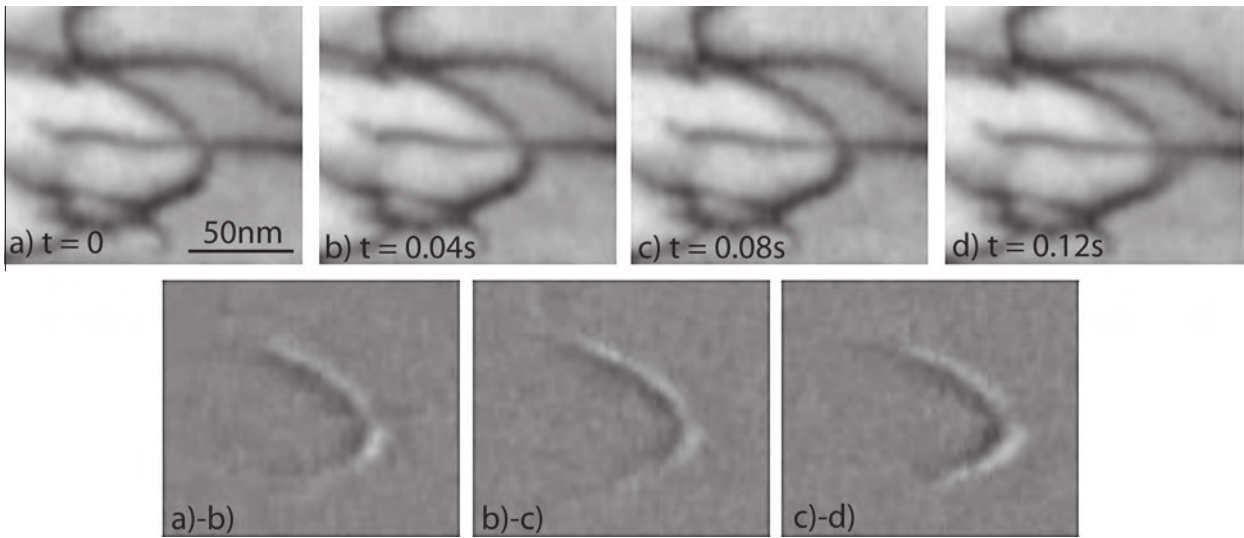


**Fig. 6.** Details of a dislocation motion in Fig. 5, showing a very steady motion at a velocity of  $\sim 200$  nm/s ( $T = 450$  °C).

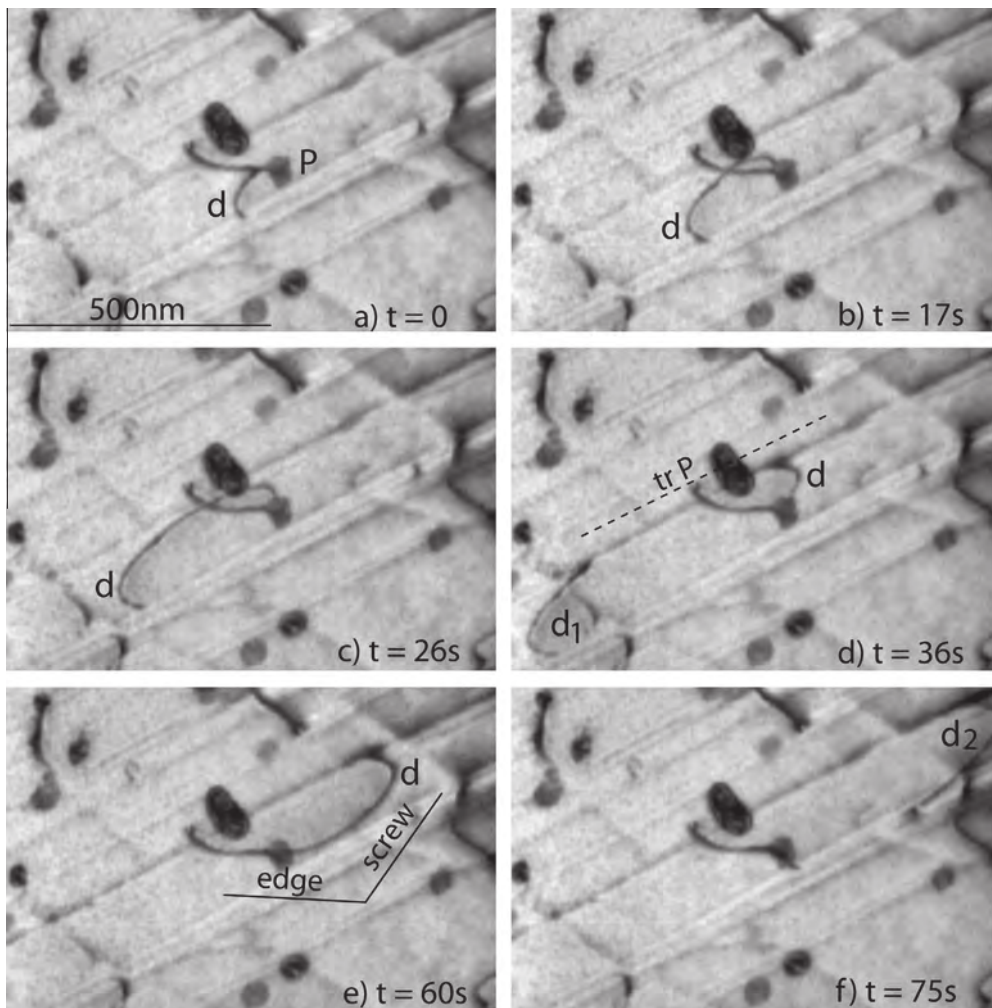


**Fig. 7.** Dislocation source, in sample 2 (grain 1) deformed at 400 °C. The dislocation arm  $d$  rotates clockwise around the precipitate  $P$ , and emits  $d_1$  to the left and  $d_2$  to the right. The rectilinear slip trace noted  $trP$  indicates a pure slip in a prismatic plane. Edge and screw directions are shown in projection in the observation plane. Diffraction vector  $(\bar{1}011)$ . The corresponding video can be downloaded as a [Supplementary material](#).

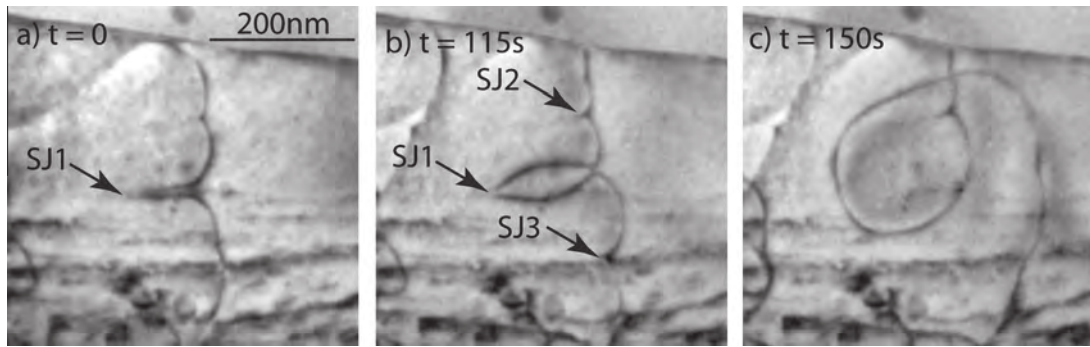


**Fig. 8.** Pinning at super-jogs in sample 2 (grain 2), strained at 400 °C. A dislocation anchored at a super-jog noted SJ1 trails a dipole (in (a)). The dipole subsequently opens (in (b)) and forms a new dislocation loop (in (c)). Other super-jogs are noted SJ2 and SJ3. Diffraction vector ( $10\bar{1}1$ ). The corresponding video can be downloaded as a [Supplementary material](#).

between their ( $0\bar{1}10$ ) prismatic plane (Schmid factor 0.2) and either the most activated ( $0\bar{1}11$ ) first-order pyramidal plane (Schmid factor 0.29) or the basal plane (Schmid factor 0.25). By comparison with grain 1, this shows that a non-prismatic slip is activated only when its resolved shear stress is higher than that of the concurrent prismatic plane, namely that the critical resolved shear stress of the non-prismatic slip is probably slightly higher than that of the prismatic one. The exact nature of non-prismatic slip (pyramidal or basal) cannot however be unambiguously determined at the fine scale in this specific case. For more extending deviations, *ex-situ* observations of Rautenberg et al. support that the first-order pyramidal plane is the common deviation plane [21].

As a result of this abundant cross-slip, many super-jogs similar to those described in [16] are continuously created and eliminated on mobile dislocations. For instance, Fig. 8 shows a dislocation  $1/3[2\bar{1}\bar{1}0]$  anchored at a super-jog SJ1, trailing a dipole which subsequently opens and forms a large expanding loop. Such a process has been referred as a multiplication at an open loop in another hcp metal [24].

The other pinning points, noted SJ2 and SJ3, are also super-jogs, as shown in Fig. 9. Indeed, Fig. 9 shows another dislocation of the same type, anchored at a super-jog SJ. This super-jog moves downward as the dislocation glides to the right, thus allowing the dislocation to escape from the corresponding pinning point. The jog motion takes place along the Burgers vector direction, which can only be explained by the pure glide process described in Fig. 9d. The driving force for the side motion of the super-jog is the difference in the line-tension forces exerted by the two arms along the screw direction. Neither jog motion in other directions nor dipole annihilation which would require climb has been observed at this temperature.

### 3.2. Dislocation velocity versus stress measurements at 400 °C

This section is devoted to the stress-dependence of the dislocation velocity and associated strain-rate. In the first part, the dislocation velocity is shown to follow the power-law  $v \propto \tau^n$  with  $\tau$  the applied stress and  $n \sim 4.3$ . In a second part, the same velocity is shown to be proportional to the local driving stress ( $v \propto \tau$ ). The apparent discrepancy between these two stress dependences results from the two

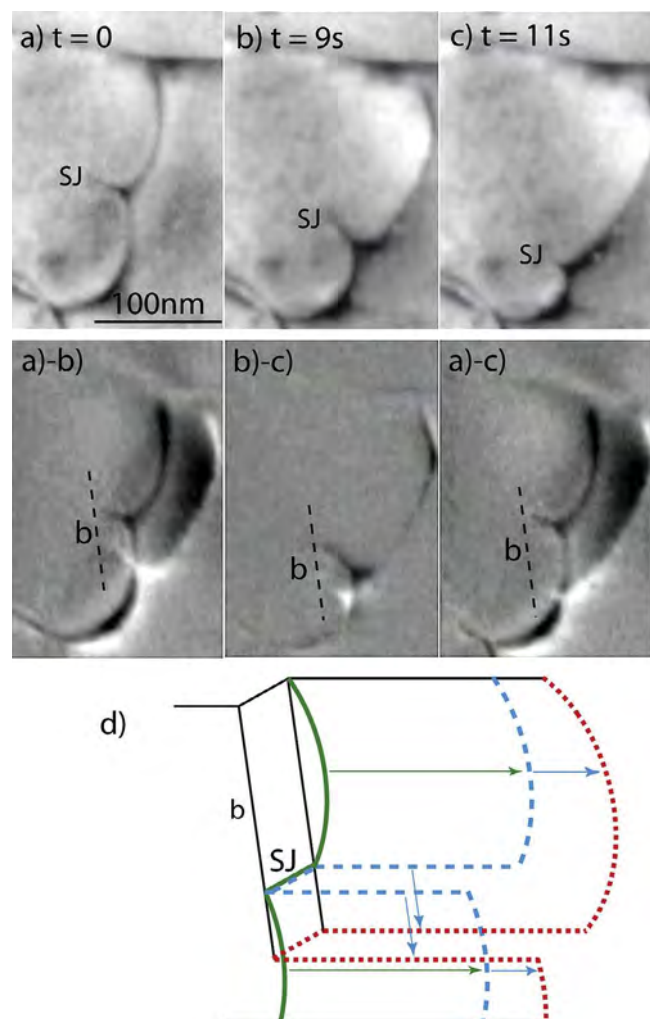


**Fig. 9.** Formation and motion of a dipole connected to a super-jog SJ (same area as in Fig. 8, 400 °C). The motion takes place by glide along the Burgers vector direction  $b$ , according to the scheme in (d). The corresponding video can be downloaded as a [Supplementary material](#).

different stresses involved at different scales (applied stress in the first case, local driving stress opposed to the friction stress in the second case). This result is a new illustration of the importance to consider the impact of the transition scales in viscoplastic description of Zr alloys behavior.

### 3.2.1. Dislocation velocity as a function of applied stress

The dynamic sequence Fig. 10 yields an order of magnitude of the stress-dependence of the dislocation velocity. Still in grain 2 of sample 2, two dislocation systems are activated simultaneously: the preceding one, consisting of  $1/3[2\bar{1}\bar{1}0]$  dislocations gliding in  $(0\bar{1}10)$  and either  $(0\bar{1}\bar{1}1)$  or  $(0001)$  planes, and another one corresponding to dislocation  $d$  with a  $1/3[\bar{1}\bar{1}20]$  Burgers vector gliding in the  $(1\bar{1}00)$  prismatic plane (the slip traces on the two surfaces are noted trP). These two systems have very different Schmid factors, respectively 0.2 in P/0.29 in  $\pi/0.25$  in B (first system) and 0.47 in P (second system), to which correspond very different velocities. More precisely, the velocity of  $d$  is about 20 times higher than that of the other dislocations (40 nm/s versus 2 nm/s), for a resolved shear stress about twice higher. This can be described by a power law  $v \propto \tau^n$ , with  $\tau$  the resolved shear stress and  $n \sim \ln 20 / \ln 2 \sim 4.3$  (with a large uncertainty). This value is smaller

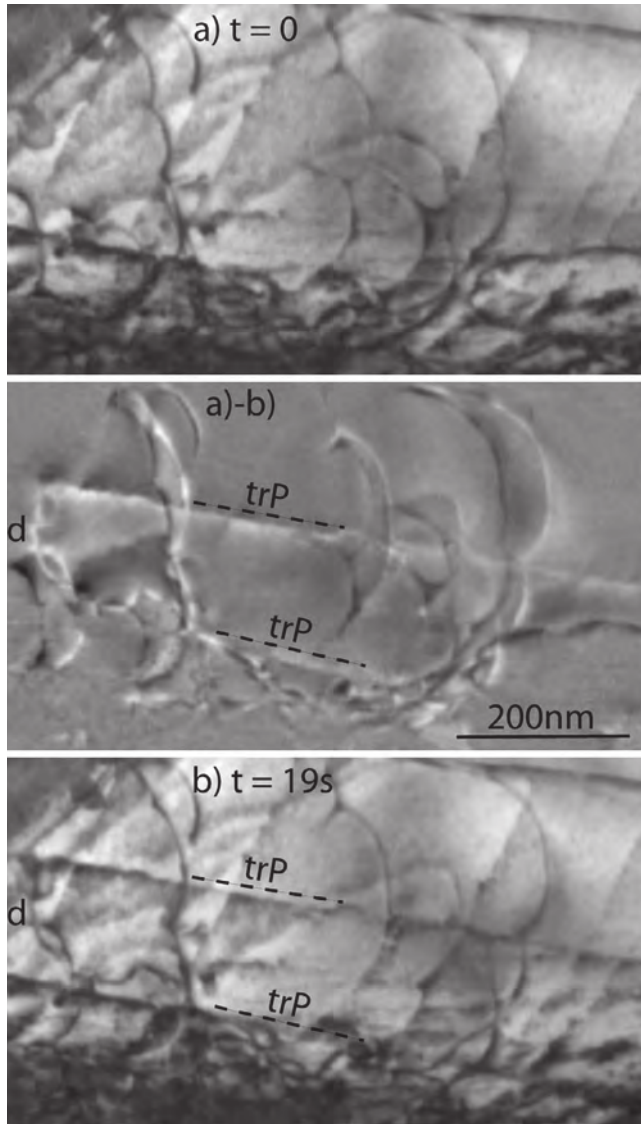


**Fig. 10.** Fast motion of dislocation  $d$  with a high Schmid factor (corresponding slip traces trP), compared to the slow motion of the other dislocations with a lower Schmid factor. Same area as in Figs. 8 and 9, 400 °C. The corresponding video can be downloaded as a [Supplementary material](#).

than but nevertheless comparable to the macroscopic value  $n \sim 6$  discussed in the introduction.

### 3.2.2. Dislocation velocity as a function of the local driving stress

The velocity law measured above is related to the applied stress, not to the total driving stress acting on individual dislocations. Since the dislocations are curved, the line tension stress  $\tau_l$  must indeed be subtracted from the applied shear stress  $\tau$ .

This line tension stress varies as the inverse of the radius of curvature according to  $\tau_l = T/Rb$ , where  $T$  is the dislocation line tension. In the isotropic elasticity approximation,  $T$  can be expressed as  $T = E + \partial^2 E / \partial \theta^2$ , where  $E$  is the dislocation line energy and  $\theta$  the dislocation character. This yields  $T = (\mu b^2 / 4\pi) [\cos^2 \theta + (\sin^2 \theta / (1 - \nu)) + (2\nu / (1 - \nu)) (\cos^2 \theta - \sin^2 \theta)] \ln R / b$ , with  $\mu$  the shear modulus,  $\nu$  the Poisson ratio, and  $R$  the outer cut-off radius. For edge and screw parts, the ratio of the line tensions is thus  $T_s / T_e = (1 + \nu) / (1 - 2\nu)$ .

Under such conditions, the equilibrium shape of a dislocation loop under stress is an ellipse with a ratio of maximum to minimum elongation (in screw and edge directions respectively)  $a/b = [(1 + \nu) / (1 - 2\nu)]^{1/3} = 1.58$ , and a ratio of maximum to minimum radii of curvature  $R_e / R_s = (1 + \nu) / (1 - 2\nu) = 3.9$ .

Very similar results are given by the software DISDI based on anisotropic elasticity calculations [25]. According to these latter results, and using elastic constants at 400 °C [26,27], we obtain  $\tau_l$  (MPa) = 11200/ $a$ (nm) = 7400/ $b$ (nm), where  $a$  and  $b$  are the maximum and minimum ellipse elongations verifying  $a/b \sim 1.51$ .

In the absence of any friction stress, the equilibrium between line tension stress and applied shear stress can be written  $\tau_l = \tau$ . When dislocations are subjected to a friction stress  $\tau_f$ , this equation must however be replaced by  $\tau_l = \tau - \tau_f$ , i.e. the applied shear stress must be decreased by the friction stress  $\tau_f$ .

The friction stress can a priori depend on several parameters, (i) the dislocation character, and (ii) the dislocation velocity, when the motion is thermally activated. In the first case, the equilibrium shape is no more the ellipse described above, and in the second case the dynamic equilibrium shape of a moving dislocation depends on its velocity, which obviously makes the analysis trickier. These two dependences are studied in what follows.

#### 3.2.2.1. Dynamic equilibrium shape of mobile loops

All images have been treated in order to correct from perspective effects, i.e. dislocations are seen as if the observation plane was their gliding plane. Then, dislocations nicely curved between two anchoring points are compared with ellipses of different sizes and different  $a/b$  ratios. One example is shown in Fig. 11, where  $a/b = 1.52$ . In all cases the ratio  $a/b$  ranges between 1.4 and 1.7, close to the equilibrium value  $a/b = 1.5$  calculated above, which shows that the friction force is either zero, or almost independent of the dislocation character.

#### 3.2.2.2. Friction stress as a function of dislocation velocity

Fig. 12 shows an expanding loop subjected to a resolved applied shear stress  $\tau$  which can be considered constant



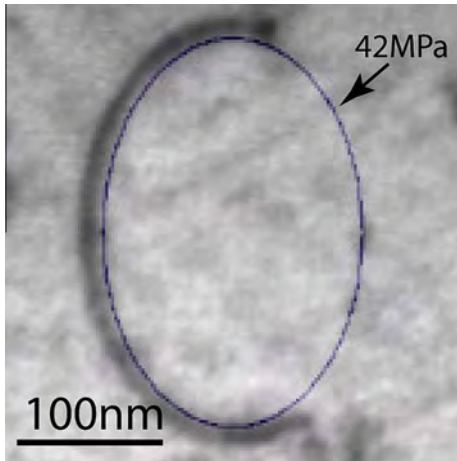


**Fig. 11.** Dislocation curved between two pinning points at 400 °C, compared with a loop shape computed in anisotropic elasticity under a stress of 42 MPa. The image is corrected from perspective effects.

during the short time of the sequence. The loop shape has been corrected from perspective effects, and from the shift between the real dislocation position and its image (which depends on the sign of the diffraction vector). This shape is approximated by ellipses of various sizes but constant  $a/b$ , which allows one to measure the line tension stress  $\tau_l$  as a function of the dislocation velocity  $v$ . Fig. 12i shows that this variation is linear, which, according to  $\tau_l = \tau - \tau_f$ , implies that  $\tau_f$  is proportional to  $v$ . In other words, the dislocation velocity  $v$  is proportional to the “driving” stress (opposed to the friction stress  $\tau_f$ ) responsible for the motion. Under such conditions, and since by definition the friction stress tends to zero when the velocity tends to zero, extrapolating the straight line to  $v = 0$  yields the local value of the applied

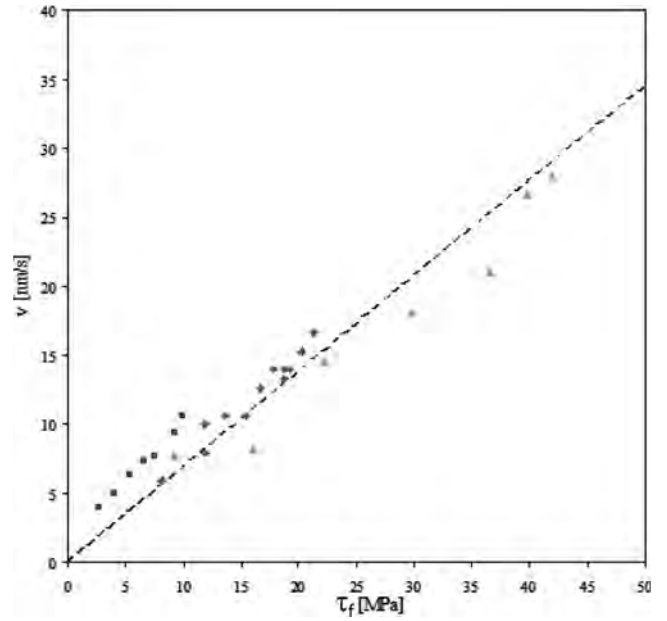


**Fig. 13.** Dislocation velocities as a function of friction stress. The three symbols correspond to three different measurements.

shear stress,  $\tau = 50$  MPa. Since the Schmid factor of this slip system is about 0.25 (average between 0.2 for the prismatic plane, 0.29 for the pyramidal plane, and 0.25 for the basal plane), this corresponds to an applied stress of about 200 MPa (and 120–150 MPa for the other cases studied), in consistency with macroscopic values deduced from conventional mechanical tests at comparable strain rates (between 120 and 160 MPa) [28]. Several velocity versus friction stress measurements performed in several grains all yield the same proportionality law, as shown in Fig. 13.

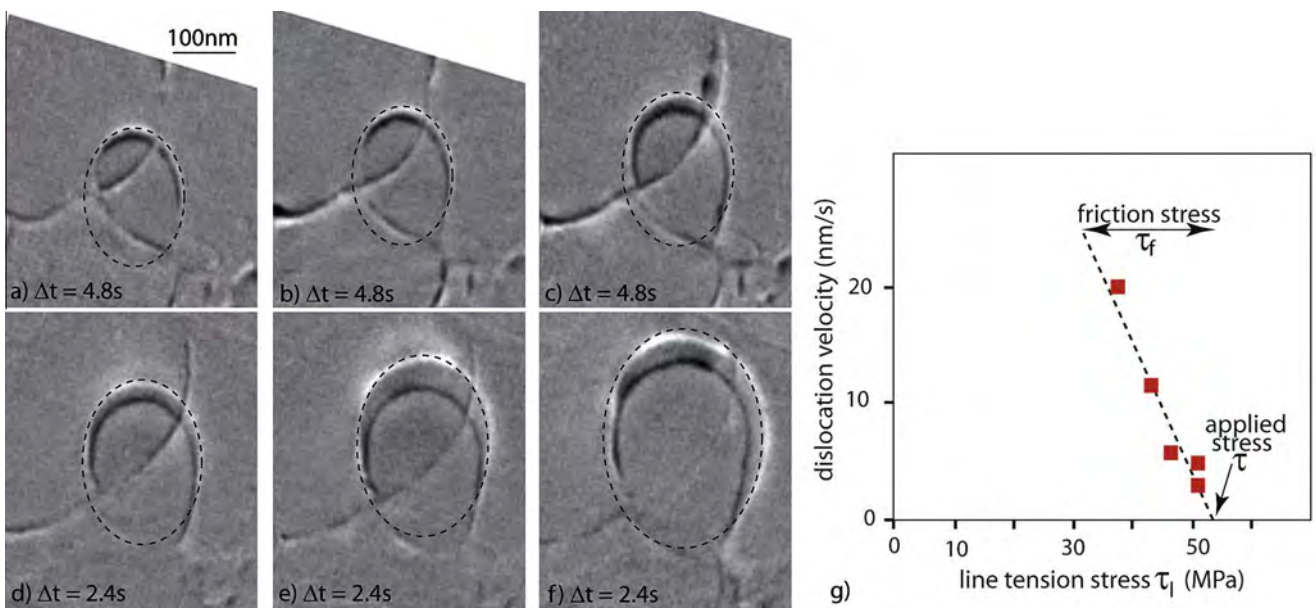


**Fig. 12.** Loop expansion as a function of time increment, and corresponding glide velocity as a function of line-tension stress (deduced from theoretical equilibrium loop shapes). The images are differences between frames separated by times  $\Delta t$ , corrected from perspective effects. Sample 2, grain 2, 400 °C, diffraction vector  $(10\bar{1}1)$ . The corresponding video can be downloaded as a [Supplementary material](#).

#### 4. Discussion

The first important result of this study is the observation of DSA at the scale of individual dislocations. Indeed, several *in situ* measurements in samples with various grain orientations consistently show a particular kinetics of mobile dislocations at 350 °C. Whereas dislocations move homogeneously and steadily below and above this temperature, their motion is very irregular and either very slow or very fast, as if intermediate velocities were forbidden. This picture corresponds to what is expected from DSA, as observed previously in the intermetallic alloys TiAl and Fe<sub>3</sub>Al [29], and in iron with carbon [30], under similar conditions.

Fast dislocations at 350 °C accordingly move by a low-temperature mechanism, namely the crossing of immobile solute atoms (in agreement with Fig. 2), whereas slow ones at the same temperature move by a high-temperature mechanism, namely the diffusion-controlled dragging of solute atoms. Under such conditions, intermediate dislocation velocities are not allowed, because of a too fast solute diffusion for the low-temperature mechanism, and a too slow solute diffusion for the high-temperature one.

The observation of DSA at the scale of individual dislocations in a thin foil is a nice confirmation of the reliability of *in situ* experiments. As mentioned in the introduction, a direct consequence of DSA is the occurrence of solute dragging at higher temperatures. This point will be discussed later.

The second important result is the role of superjogs, which are created by double cross-slip between prismatic and either pyramidal and/or basal planes, probably at the vicinity of solute atoms according to [31]. The landscape of curved dislocations pinned at superjogs is identical to that observed *post-mortem* by Moon et al. [16] and Rautenberg et al. [21], which again confirms the reliability of *in situ* experiments. However, and contrary to what has been postulated in reference [16], superjogs do not move by climb, which rules out the interpretation of the plastic properties by the jog-dragging mechanism. On the contrary, superjogs move along the Burgers vector direction by pure glide, under line tension forces arising from the curvature of mobile dislocation arcs (Fig. 9d). Similar “unzipping” processes have already been postulated and observed in other materials [32,33]. Under such conditions, the larger bowing dislocation arcs grow at the expense of the smaller ones, and superjogs are swept to dislocation extremities, until new superjogs are formed by cross-slip. As a result of this dynamic equilibrium, the motion of dislocations can be described by the viscous glide of curved loops, of average size scaling with the mean distance between superjogs. Thermal activation thus originates from the intrinsic glide mechanism between pinning points.

Although the present results do not support the theory of climb-controlled dislocation motion at 400 °C, other diffusion-controlled mechanisms are rate-controlling at this temperature. Indeed, the measurements of Section 3.2.2 show that the glide velocity varies proportionally to the total driving stress (opposed to the friction stress  $\tau_f$ ), equal to the local applied shear stress  $\tau$  minus the line tension stress  $\tau_l$ . Such a behavior corresponds exactly to the solute dragging mechanism expected above the DSA domain. Indeed, according to Friedel [34], the dislocation velocity can be written  $v = (2b^2D/kT)\tau$ , where

$D = v_D b^2 \exp - (H_d/kT)$  is the diffusion coefficient of the solute atoms responsible for DSA (presumably oxygen),  $v_D$  is the Debye frequency, and  $H_d$  is the corresponding enthalpy of diffusion. From the slope of Fig. 13, we can deduce  $D \sim 3.3 \cdot 10^{-17} \text{ m}^2/\text{s}$  and  $H_d \sim 1.31 \text{ eV}$ . This activation energy is substantially lower than that corresponding to the diffusion of oxygen in zirconium, of the order of 1.9 eV according to [35,36]. However, our experimental value corresponds to the diffusion of atoms located in, or close to the dislocation core which, like the pipe diffusion (which takes place along the dislocation line, not perpendicular to it), could be easier than in the undistorted lattice.

It can be noted that in the Friedel approximation, the dislocation velocity is independent of the solute concentration in the dislocation core, namely independent of the dislocation character, in agreement with the experimental results.

This velocity law is however not directly transmitted to the whole microsample. Indeed, Fig. 10 shows that the average dislocation velocity follows a power law of the type  $\bar{v} = \tau^n$  with  $n$  larger than unity ( $n \sim 4.3$ ), in agreement with macroscopic results. This apparent discrepancy is discussed below.

Instead of discussing the behavior of individual dislocations, under a constant applied stress  $\tau$  and a variable line-tension stress  $\tau_l$  (as in Figs. 12 and 13), we now consider the average property of a large dislocation ensemble. These dislocations are subjected to an average line-tension stress  $\bar{\tau}_l$  which can be considered constant (of the order of 40 MPa according to Fig. 12), and to an applied stress  $\tau$  varying with the applied strain-rate. The average dislocation velocity is still proportional to  $\tau - \bar{\tau}_l$ . However, this velocity can also be written  $\bar{v} = \tau^n$ , with  $n = [\Delta \ln(\tau - \bar{\tau}_l) / \Delta \ln \tau]$ , which, for  $\bar{\tau}_l = 40 \text{ MPa}$  and  $\tau$  varying between 45 MPa and 60 MPa, yields  $n \sim 5$  in agreement with Fig. 10 and macroscopic results.

In these estimates, the line tension stress plays the same role as the threshold stress which is often put forward to account for high creep exponents in phase-dispersed alloys [37–39]. A general expression proposed by Çadek [38] yields in the present case:

$$n = \frac{\tau}{\tau - \bar{\tau}_l} \left( 1 - \frac{\partial \bar{\tau}_l}{\partial \tau} \right)$$

This expression takes into account the variation of the threshold stress with applied stress, which may result from the lateral glide motion of super-jogs. Our *in situ* observations are not accurate enough to measure such possible effects, but their implementation in a polycrystal-line model would probably result in a more comprehensive modeling.

#### 5. Conclusions

*In situ* straining experiments in a zirconium alloy have yielded the following results:

- Dynamic strain aging (DSA) has been observed at the scale of individual dislocations, at the same temperature of 350 °C as in macroscopic mechanical tests. It is characterized by an inhomogeneous deformation by a series of very fast individual dislocation movements, mostly in prismatic planes.
- Above and below this temperature, the deformation proceeds by a homogeneous and steady dislocation motion.

- At 400 °C, curved dislocation loops are anchored at super-jogs formed by double cross-slip between prismatic and either pyramidal or basal planes. These super-jogs move by glide along the Burgers vector direction, which rules out models based on the climb motion of jogs/super-jogs on screw dislocations.
- Dislocations gliding between anchoring points (precipitates and/or superjogs) are subjected to a friction stress which is almost independent of the character (edge/screw).
- When the line-tension stress is subtracted from the applied shear stress, the resulting driving stress (opposite to the friction stress) is proportional to the dislocation velocity. Such a behavior is consistent with the solute dragging mechanism expected above the DSA temperature regime.
- The average dislocation velocity as a function of applied stress can be expressed by a power-law with  $n > 1$  ( $n \sim 4$  according to one estimate), in agreement with results from mechanical tests. The apparent discrepancy with the proportionality law of solute dragging results from the line-tension stress which plays the role of a threshold stress.

#### Acknowledgements

The authors are indebted to Philippe Pilvin, Dominique Poquillon and Jean-Marc Cloué for stimulating the studies of creep mechanisms in zirconium alloys. The experiments have been funded by AREVA NP through the French METSA program.

#### Appendix A. Supplementary data

Supplementary data associated with this article can be found, in the online version, at <http://dx.doi.org/10.1016/j.actamat.2015.01.016>.

#### References

[1] D. Mills, G.B. Craig, *Trans. Met. Soc. AIME* 242 (1968) 1881.  
 [2] J.L. Derep, S. Ibrahim, R. Rouby, G. Fantozzi, *Acta Met.* 28 (1980) 607.  
 [3] Z. Trojanova, P. Lukac, A. Dlouhy, H.J. Heinitz, *Czech J. Phys.* B35 (1985) 298.  
 [4] Z. Trojanova, A. Dlouhy, P.J. Lukac, *Mater. Sci.* 30 (1995) 2930.  
 [5] P. Geyer, Ph.D., Ecole des Mines de Paris, 1999.

[6] S.I. Hong, *Mater. Sci. Eng.* 79 (1986) 1.  
 [7] P. Delobelle, P. Robinet, P. Geyer, P. Bouffieux, *J. Nucl. Mater.* 238 (1996) 135.  
 [8] S. Graff, Ph.D., Ecole des Mines de Paris, 2006.  
 [9] W.R. Thorpe, I.O. Smith, *J. Nucl. Mater.* 75 (1978) 209.  
 [10] N. Rupa, Ph.D., Université de Technologie de Compiègne, France, 2000.  
 [11] C. Nam, B.K. Choi, M.H. Lee, Y.H. Jeong, *J. Nucl. Mater.* 305 (2002) 70.  
 [12] T.A. Hayes, M.E. Kassner, R.S. Rosen, *Metall. Mater. Trans. A* 33A (2002) 337.  
 [13] T.A. Hayes, M.E. Kassner, *Metall. Mater. Trans. A* 37A (2006) 2389.  
 [14] S.R. Mc Ewen, R.G. Fleck, O.T. Woo, *Metall. Trans. A* 12A (1981) 1751.  
 [15] H. Siethoff, K. Ahlborn, *Scripta Met.* 21 (1987) 1439.  
 [16] J.H. Moon, P.E. Cantowine, K.R. Anderson, S. Karthikeyan, M.J. Mills, *J. Nucl. Mater.* 353 (2006) 177.  
 [17] K.L. Murty, B.L. Adams, *Mater. Sci. Eng.* 70 (1985) 169.  
 [18] I. Charit, K.L. Murty, *J. Nucl. Mater.* 374 (2008) 354.  
 [19] C. Grosjean, D. Poquillon, J.C. Salabura, J.M. Cloué, *Mater. Sci. Eng. A* 510–511 (2009) 332.  
 [20] M. Priser, M. Rautenberg, J.M. Cloué, P. Pilvin, X. Feaugas, D. Poquillon, *J. ASTM Int.* 8 (2011) 10.  
 [21] M. Rautenberg, X. Feaugas, D. Poquillon, J.M. Cloué, *Acta Mater.* 60 (2012) 4319.  
 [22] J.P. Mardon, G.L. Garner, P.B. Hoffmann, In: *Proceedings of the 2010 LWR fuel performance meeting*, Orlando, 2010.  
 [23] M. Rautenberg, D. Poquillon, P. Pilvin, C. Grosjean, J.M. Cloué, X. Feaugas, *Nucl. Eng. Des.* 269 (2014) 33.  
 [24] A. Couret, D. Caillard, *Acta Met.* 33 (1985) 1447–1455.  
 [25] J. Douin, P. Veyssière, P. Beauchamp, *Philos. Mag. A* 54 (1986) 375.  
 [26] E.S. Fisher, C.J. Renken, *Phys. Rev.* 135 (1964) A482.  
 [27] M. Tremblay, C. Roy, *Mater. Sci. Eng.* 12 (1973) 235.  
 [28] M. Rautenberg, Ph.D., Université de Toulouse, France, 2012.  
 [29] G. Molénat, A. Couret, D. Caillard, *Mater. Sci. Eng. A* 234–236 (1997) 660.  
 [30] D. Caillard, J. Bonneville, *Scripta Mater.* 95 (2015) 15.  
 [31] D. Caillard, M. Legros, A. Couret, *Philos. Mag.* 93 (2013) 203.  
 [32] B. Viguier, K.J. Hemker, J. Bonneville, F. Louchet, J.L. Martin, *Philos. Mag.* A71 (1995) 1295.  
 [33] D. Caillard, *Acta Mater.* 61 (2013) 2808.  
 [34] J. Friedel, *Dislocations*, Pergamon, 1964.  
 [35] I.G. Richtie, A. Atrens, *J. Nucl. Mater.* 67 (1977) 254.  
 [36] B. Li, A.R. Allnett, C.S. Zhang, P.R. Norton, *Surf. Sci.* 330 (1995) 276.  
 [37] H.E. Evans, G. Knowles, *Metal Sci.* 14 (1980) 262.  
 [38] J. Cadek, *Mater. Sci. Eng.* 94 (1987) 79.  
 [39] J. Cadek, H. Oikawa, V. Sustek, *Mater. Sci. Eng. A* 190 (1995) 9.